THE JOURNAL OF PHYSICAL CHEMISTRY C

pubs.acs.org/JPCC

Article

Electronic Structure and Interface Energetics of $CuBi_2O_4$ Photoelectrodes

Freddy E. Oropeza,* Nelson Y. Dzade, Amalia Pons-Martí, Zhenni Yang, Kelvin H. L. Zhang, Nora H. de Leeuw, Emiel J. M. Hensen, and Jan P. Hofmann*

Cite This: *J. Phys. Chem. C* 2020, 124, 22416−22425

Read Online

ACCESS | Metrics & More | Article Recommendations | Supporting Information

ABSTRACT: $CuBi_2O_4$ exhibits significant potential for the photoelectrochemical (PEC) conversion of solar energy into chemical fuels, owing to its extended visible-light absorption and positive flat band potential vs the reversible hydrogen electrode. A detailed understanding of the fundamental electronic structure and its correlation with PEC activity is of significant importance to address limiting factors, such as poor charge carrier mobility and stability under PEC conditions. In this study, the electronic structure of $CuBi_2O_4$ has been studied by a combination of hard X-ray photoemission spectroscopy, resonant photoemission spectroscopy, and X-ray absorption spectroscopy (XAS) and compared with density functional theory (DFT) calculations. The photoemission study indicates that there is a strong Bi 6s−O 2p hybrid electronic state at 2.3 eV below the Fermi level, whereas the valence band maximum (VBM) has a predominant Cu 3d−O 2p hybrid character. XAS at the O K-edge supported by DFT calculations provides a good description of the conduction band, indicating that the conduction band minimum is composed of unoccupied Cu 3d−O 2p states. The combined experimental and theoretical results suggest that the low charge carrier mobility for $CuBi_2O_4$ derives from an intrinsic charge localization at the VBM. Also, the low-energy visible-light absorption in $CuBi_2O_4$ may result from a direct but forbidden Cu d−d electronic transition, leading to a low absorption coefficient. Additionally, the ionization potential of $CuBi_2O_4$ is higher than that of the related binary oxide CuO or that of NiO, which is commonly used as a hole transport/extraction layer in photoelectrodes. This work provides a solid electronic basis for topical materials science approaches to increase the charge transport and improve the photoelectrochemical properties of $CuBi_2O_4$-based photoelectrodes.

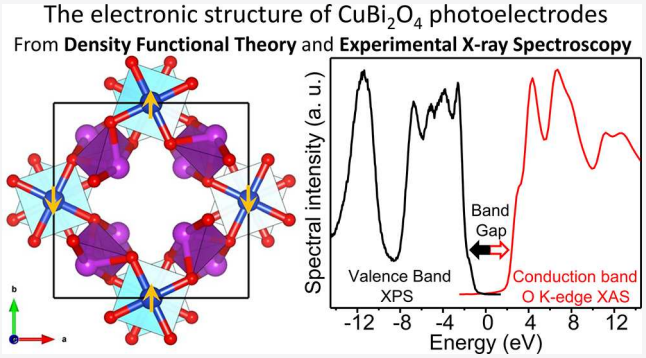

INTRODUCTION

The tetragonal copper bismuth oxide $CuBi_2O_4$ has a crystal structure that features a three-dimensional array of $[CuO_4]^{6-}$ square-planar units, staggered along the *c*-axis and separated by Bi^{3+} ions, as shown in Figure S1 of the Supporting Information (SI). Such a crystal structure isolates the $[CuO_4]^{6-}$ units from each other, in contrast to the crystalline structure of the isoelectric prototypical high-temperature superconducting (HTSC) cuprates CuR_2O_4 (where R is a trivalent rare-earth element), in which the $[CuO_4]^{6-}$ square-planar units form infinite two-dimensional layers.[1] Since this structural feature is a fundamental characteristic of HTSC cuprates, $CuBi_2O_4$ with its characteristic isolated $[CuO_4]^{6-}$ units is unlikely to show superconductivity. However, $CuBi_2O_4$ has been shown to have potential use as a material for the photoelectrochemical (PEC) conversion of solar energy into chemical fuels.[2−4] Photocathodes based on this material have been shown to generate photocurrent densities on the order of −1.0 mA/cm^2 at 0.0 V vs the reversible hydrogen electrode (RHE) with a Faradaic efficiency for hydrogen evolution of ∼91%.[5] In the ternary oxide $CuBi_2O_4$, the hybridizations of Bi 6s states and Cu 3d states with O 2p within the valence and conduction bands are key factors that cause the desirable materials properties, such as visible-light absorption as well as p-type conductivity.[2] Therefore, knowledge of the elemental composition of the valence band maximum (VBM) can provide fundamental guidance to materials design that could lead to further improvement of their properties.

Similar to other copper-based oxides, the major drawbacks limiting the PEC performance of $CuBi_2O_4$ are the lack of stability against photocorrosion when in contact with aqueous electrolytes and the poor charge carrier transport properties.[2,3] These limitations mean that the development of $CuBi_2O_4$-

Received: September 16, 2020
Published: September 30, 2020

based photoelectrodes will depend on the optimization of interfacial electric contacts with protection layers and charge transport layers that assist the separation of photogenerated charges. Since the charge transfer across interfaces plays a major role in the overall efficiency of multilayer photoelectrodes, the engineering of interface energetics is key to overcome efficiency losses due to unfavorable charge carrier dynamics and transport. The optimization of the interfaces is ultimately based on the electronic properties of $CuBi_2O_4$, and therefore, a detailed determination of the electronic structure is needed in order to guide the rational design of stable and high-performing photoelectrodes. Herein, we report a comprehensive description of the electronic structure and electron energetics in $CuBi_2O_4$ using a combination of X-ray photoemission spectroscopy (XPS), X-ray absorption spectroscopy (XAS), and density functional theory (DFT) calculations.

The electronic structure of $CuBi_2O_4$ has been the subject of a number of theoretical studies based on DFT calculations,[2,6,7] which generally agree that the Bi 6s and Cu 3d electrons contribute to the valence band through hybrid electronic states with O 2p. However, there are diverging suggestions regarding the energy levels of the contributions of the metal orbitals to the valence band. Whereas calculations by Sharma et al.[2] suggested that Bi 6s and Cu 3d have comparable contributions to the valence band maximum (VBM), the results presented by Janson et al.[6] and Di Sante et al.[7] suggest that the Bi contribution to the VBM is in fact negligible, so that an effective one-band model is appropriate for the description of the low-lying excitations in $CuBi_2O_4$. Several studies of the electronic structure of HTSC cuprates have established that calculations using $[CuO_4]^{6-}$ clusters with D_{4h} symmetry as models accurately describe electronic features and soft X-ray photoemission spectra of low-dimensional cuprates, because these models take into account configurations, interactions, and final states with more than one d hole (i.e., Cu $3d^8$).[8−10] For $[CuO_4]^{6-}$ clusters, the excitation of low-lying energy levels (i.e., the VBM) is associated with the antiferromagnetic coupling of O 2p holes with Cu $3d^9$ that leads to a singlet state ($3d^9\underline{L}$, $\underline{L}$ = ligand hole), usually referred to as the Zhang-Rice single state.[9,10] Due to the hybridization with d^8 and d^{10} $\underline{L}^2$ configurations, this singlet state has a large stabilization energy and strongly affects the physicochemical properties of cuprates, e.g., the charge mobility and doping stability.

Spectral features related to Zhang−Rice singlet states have been clearly identified in the valence band photoemission spectrum of CuO.[8,11,12] However, spectroscopic signatures of this singlet have not been observed in the photoemission spectrum of $CuBi_2O_4$,[13,14] which thus brings into question its stability within this material. In early experimental work, Goldoni et al. described $CuBi_2O_4$ as a charge-transfer insulator on the basis of their photoemission data, but no spectroscopic evidence of a Zhang−Rice singlet state was found.[14] Since the photoionization cross sections of the Bi valence states are too low compared to those of Cu 3d at the soft X-ray excitation energies that they used, the Bi contribution to the valence band could not be directly observed in the photoemission data. However, the Bi contribution to the valence band was addressed from the interpretation of electronic transitions observed in the electron energy loss spectroscopy data, which suggested that Bi 6s contributes to the top of the valence band.

In this paper, we report a detailed study of the electronic structure of $CuBi_2O_4$ based on an advanced and comprehensive X-ray spectroscopic approach, combining hard X-ray photoemission spectroscopy (HAXPES), resonant photoemission spectroscopy (ResPES), O K-edge XAS, and first-principles DFT calculations. Although photoionization cross sections of all electronic orbitals decrease as a function of the ionizing photon energy, the relative values are very different in the soft and hard X-ray regimes. As a result, soft X-ray photoemission spectroscopy preferentially probes Cu 3d valence states, whereas Bi 6s and Bi 6p make up most of the spectral features in HAXPES. This distinction allows identification of the Bi and Cu contributions to the valence band by taking valence band spectra at different ionization photon energies. We present an analysis of the optoelectronic properties of $CuBi_2O_4$ based on its electronic structure, concluding that the low visible-light absorption coefficient may come from a localized d−d forbidden electronic transition, leading to a low absorption coefficient in this spectral range and poor photochemical activity under low-energy visible-light irradiation. Additionally, a combined experimental and theoretical study of the electron energetics shows that the ionization potential (IP) of $CuBi_2O_4$ is higher than that of the related material CuO and that of NiO, which is the electronic basis for current materials science approaches to tailor charge carrier transport properties of $CuBi_2O_4$-based photoelectrodes.

EXPERIMENTAL SECTION

Sample Preparation. Samples were prepared by a spin-coating technique. Bismuth nitrate pentahydrate (Sigma-Aldrich, ≥99.99%) and copper nitrate trihydrate (Sigma-Aldrich, 99.999%) were dissolved in a solvent comprising a mix of acetic acid−water−2-methoxyethanol in a 2:1:1 volume ratio, to obtain a 2.6 M total metal concentration in solution. Citric acid was added to the solution at a 1:1 molar ratio with Cu just before using it for the deposition, which works as a gelling agent in the coating solution. The resulting solutions were used to spin-coat 2 × 2 cm^2 sized fluorine-doped tin oxide (FTO) substrates at 3000 rpm. Prior to coating, the substrates were cleaned by ultrasound rinsing in acetone and then ethanol, followed by a UV/ozone cleaning treatment for 15 min. After coating, substrates were directly placed in a furnace at 450 °C and after 2 h the furnace was allowed to cool down naturally to room temperature, which led to the formation of a single-phase $CuBi_2O_4$ thin film as confirmed by XRD analysis (see Figure S1, SI).

The same procedure was used to prepare CuO. In this case, however, the solution concentration was 1.3 M copper nitrate trihydrate (Sigma-Aldrich, 99.999%).

For the nickel oxide hole transport layer, nickel nitrate hexahydrate (Sigma-Aldrich 99.999%) was dissolved in a 5:2 v:v solution of acetic acid−water to yield 5 mL of a 0.5 M solution. This solution was further diluted with 2.5 mL of 2-metoxyethanol and the resulting solution was used to spin-coat 2.5 × 2.5 cm^2 sized FTO substrates at 3000 rpm. A mask made of sticky tape was used for selective area deposition of NiO, so that the same substrate had areas of bare FTO and areas covered by NiO. Prior to coating, the substrates were cleaned by ultrasound rinsing in acetone and then ethanol, followed by a UV/ozone cleaning treatment for 15 min. After coating, the substrates were calcined for 2 h at 500 °C to form single-phase NiO. After cooling naturally to room temperature, the samples were blown with nitrogen and cleaned with a UV/ozone treatment for 15 min, prior to the copper bismuthate layer

https://dx.doi.org/10.1021/acs.jpcc.0c08455
J. Phys. Chem. C 2020, 124, 22416−22425

addition, which was prepared as detailed before for the copper bismuthate samples on the FTO supports.

X-ray Diffraction and UV−Vis Spectroscopy. X-ray diffractograms were recorded with a Bruker D2 PHASER diffractometer using Cu Kα radiation. UV−vis spectra were taken using a Shimadzu UV−vis spectrophotometer with a deuterium light source (UV range) and a halogen light source (visible range). The thin film samples were measured in transmission mode using a piece of bare FTO substrate as reference and blank.

X-ray Spectroscopy. Lab-based X-ray photoemission spectra (XPS) were taken with a Thermo Scientific K-Alpha spectrometer using a 72 W monochromated Al Kα source ($h\nu$ = 1486.6 eV). The X-rays are microfocused at the source to give a spot size on the sample of 400 μm in diameter. The analyzer is a double-focusing 180° hemisphere with a mean radius of 125 mm. It is run in constant analyzer energy (CAE) mode. The pass energy was set to 200 eV for survey scans and 50 eV for high-resolution region scans. The overall energy resolution gained was 0.5 eV, and all spectra were calibrated with respect to the Au Fermi level.

Hard X-ray and resonant photoemission spectra were measured at the I09 beamline of the Diamond Light Source in Didcot, UK.[15] For the ResPES experiment, the variable soft X-ray photon energy was tuned through a plane grating monochromator, whereas a Si(111) + Si(044) double-crystal monochromator was used for hard X-ray energies fixed at 8133 and 4068 eV. An EW-4000 photoelectron analyzer (VG Scienta) with a slit width set to 0.2 mm was used to record spectra at normal emission. The Cu L-edge X-ray absorption spectra associated with the ResPES experiment were measured in total electron yield (TEY) mode. The overall energy resolution of spectra taken at 8133 and 4068 eV photon energy was 0.32 and 0.27 eV, respectively. All spectra were calibrated with respect to the Au Fermi level.

The O K-edge X-ray absorption spectra were measured on the PGM beamline of the Laboratorio Nacional de Luz Sincrotron (LNLS), Campinas, Brazil. The variable soft X-ray photon energy was tuned through a plane grating monochromator, while the XAS spectra were taken in TEY mode with an effective resolution of 0.5 eV.

Samples studied by X-ray spectroscopy may be subject to beam damage. We addressed this issue by making sure that the chemistry of the material, as probed by coreline spectra (e.g., Cu 2p or Bi 4f), remained unchanged during the experiments. We took such coreline spectra before and after the VB recording.

Photoelectrochemical Characterization. The electrolyte was prepared by mixing equal parts of 0.1 M monobasic potassium phosphate (Sigma-Aldrich, ≥99.0%) and 0.1 M dibasic potassium phosphate dihydrate (Sigma-Aldrich, ≥99.0%). The resulting electrolyte solution had a measured pH of 6.85. The sample was placed in a PEC cell (Zahner model PECC-2) with a 3 mm diameter opening and 10 mL total electrolyte volume. A 50 μL portion of hydrogen peroxide (Sigma-Aldrich, 30 wt % in H_2O) was added to the electrolyte in the cell and it was stirred thoroughly just before PEC measurements. Photoelectrochemical measurements were conducted using a Zahner Elektrik GmbH impedance measurement unit (model IM6), using a white-light-emitting diode (LED) with maximum intensity at 565 nm and 100 mW/cm^2 intensity at the sample. For the three-electrode measurements of $CuBi_2O_4$ photocathodes, the counter electrode was a Pt wire with excess surface area, and the reference electrode was Ag/AgCl (3 M NaCl). Electrochemical potentials were converted to the RHE scale considering the calibrated potential of the Ag/AgCl (3 M NaCl) electrode, +0.241 V, and the measured pH of 6.85.

Computational Details. The spin-polarized density functional theory (DFT) calculations were performed using the Vienna Ab initio Simulation Package (VASP),[16] a periodic plane wave DFT code that includes the interactions between the core and valence electrons using the project augmented wave (PAW) method.[17] The Perdew−Burke−Ernzerhof (PBE) generalized gradient approximation (GGA) functional[18] was used for geometry optimizations. To overcome the limitation of the standard GGA-PBE functional in accurately predicting the electronic band gap of semiconducting materials, the screened hybrid functional (HSE06) with 25% Hartree−Fock exchange as proposed by Heyd−Scuseria−Ernzerhof was employed to determine the electronic structures of $CuBi_2O_4$, CuO, and NiO. A plane-wave basis set with a kinetic energy cutoff of 600 eV was tested to be enough to converge the total energies of $CuBi_2O_4$, CuO, and NiO to within 10^{-6} eV, and the residual Hellmann−Feynman forces on all relaxed atoms reached 10^{-3} eV Å. A Γ-centered Monkhorst−Pack k-mesh of (5 × 5 × 7), (7 × 7 × 5), and (9 × 9 × 9) was employed to sample the Brillouin zone of $CuBi_2O_4$, CuO, NiO, respectively. The bulk $CuBi_2O_4$ material was modeled in the tetragonal structure ($P4/ncc$ [No. 130]), CuO in the monoclinic structure ($C2/c$ [No. 15]), and NiO in the rock salt structure ($Fm\bar{3}m$ [No. 225]) with antiferromagnetic spin ordering (Figures S5−S7, SI). The optimized lattice parameters for $CuBi_2O_4$ (a = b = 8.498 Å and c = 5.903 Å) show very good agreement with the experimental lattice parameters (a = b = 8.499 Å and c = 5.803 Å).[3] Similarly, the optimized lattice parameters for CuO (a = 4.648 Å, b = 3.439 Å, c = 5.170 Å) and NiO (a = 4.209 Å) are all in close agreement (within 2% error) with reported experimental values[18,19] and previous theoretical values obtained with the PBE functional with and without the Hubbard (DFT+U) correction.[21,22]

In order to align the energies to the vacuum level, a slab-gap model was constructed and the corresponding electrostatic potential was averaged along the c-direction (see Figures S8−S10, SI), using the MacroDensity package.[23−25] The ionization potentials (IPs) were calculated when the slab vacuum level is aligned to the bulk eigenvalues, through core level eigenvalues in the center of the slab, using the O 1s orbital energy as a reference point. The electron affinity (EA) is calculated by subtracting the band gaps from the calculated ionization potentials. The work function (Φ), which is the minimum energy needed to remove an electron from the bulk of a material through a surface to a point outside the material, was calculated as $\Phi = E_v - E_F$, where E_v and E_F are the energies of the vacuum and Fermi levels, respectively. A dipole correction perpendicular to all surfaces was applied, which ensured that there is no net dipole perpendicular to the surfaces that may affect the potential at the vacuum level. To allow for easy comparison with experimental data, the photoemission spectra have been simulated using the GALORE code,[26] which extracts and interpolates the cross-sectional weights from reference data and generates tabulated data for experimental comparison. The photoionization cross sections calculated by Scofield were applied.[27] It is assumed that the contributions of atomic s-, p-, d-orbital-projected states to the total photo-

https://dx.doi.org/10.1021/acs.jpcc.0c08455
J. Phys. Chem. C 2020, 124, 22416−22425

emission spectrum will be proportional to the photoionization cross sections of corresponding orbitals in free atoms based on the Gelius model.[28,29]

RESULTS AND DISCUSSION

The experimental study of the electronic structure of $CuBi_2O_4$ was carried out with thin film samples deposited on fluorine-doped SnO_2 (FTO) by a reproducible sol−gel method described in the Experimental Section. It was ensured that no photoemission signal from the FTO substrate could be detected in the spectra of the samples, as shown in the survey spectra in Figure S2 (SI). Additionally, samples were conductive enough so that photoemission spectra were not subject to charging effects. The soft X-ray photoemission spectrum of as-prepared samples, shown in Figure S2 (SI), features intense peaks in the Bi 4f and Cu 2p regions with maxima at 158.4 and 934.1 eV, well within the expected binding energy range for Bi(III) and Cu(II) cations, respectively. The main Cu 2p peak in the spectrum of as-prepared samples, shown in detail in Figure S3 (SI), is highly symmetric, which is characteristic of $CuBi_2O_4$ and unlike CuO and other low-dimensional cuprates. Such symmetry is a consequence of the absence of nonlocal screening due to the isolation of square planar $[CuO_4]^{6-}$ species in the unit cell of $CuBi_2O_4$.[30,31]

Cu 2p Resonance in the VB Photoemission: Cu 3d Contribution to the VB. Resonant photoemission spectroscopy is a well-established technique that provides a unique means to identify the character of the various states involved in the one-electron photoemission process. This technique is powerful for solids where electron-correlation effects are expected to play an important role in the electronic structure, owing to the presence of cations with open-shell valence states (e.g., Cu^{2+}, a $3d^9$ cation) that allow intra-atomic electronic transitions.[32] In this sense, we explored the Cu 3d contribution to the valence band in detail, on the basis of the Cu 2p resonance in the valence band photoemission. Figure 1A shows valence band photoemission spectra of $CuBi_2O_4$ recorded with excitation photon energies below the onset (929.8 eV), at the onset (931.8 eV), and at the maximum (933.1 eV) of the Cu L_3 absorption edge, as indicated in Figure 1B. A very strong resonant effect can be readily observed, in particular for the high binging energy spectral features. Tuning the excitation photon energy to the maximum of the Cu L_3 edge ($h\nu$ = 933.1 eV) induces the appearance of a very strong satellite with a maximum at 13.2 eV binding energy. The resonant photoemission spectrum observed here results from the interference of two photoemission channels leading to a Cu $3d^8$ final state: (i) a direct channel (Cu $3d^9 + h\nu \rightarrow$ Cu $3d^8 + e^-$) and (ii) a deexcitation channel, which involves a photon absorption process followed by an Auger decay (Cu $3d^9 + h\nu \rightarrow$ Cu $2p^5 3d^{10} \rightarrow$ Cu $3d^8 + e^-$).[32]

The deexcitation channel only probes photoionization from Cu 3d orbitals leaving a d^8 final state and it is only available for the on-resonance spectrum. On the other hand, the direct channel also probes direct photoionization from O 2p and Bi 6s orbitals and is available at any photon energy. In view of the drastic increase of the VB spectral intensity at the Cu 2p resonance, it is clear that the deexcitation channel dominates the resonant photoemission, and therefore, the resonance reflects the contribution from Cu 3d orbitals that leave a d^8 final state upon excitation. The data show that such a contribution resides mostly at the high binding energy side

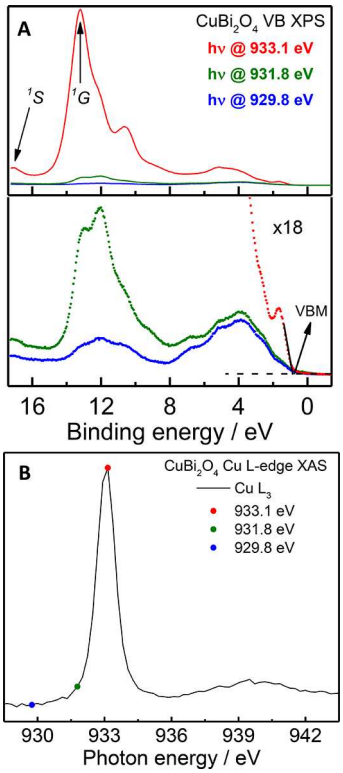

Figure 1. (A) Valence band photoemission spectra of $CuBi_2O_4$ taken using photon energies near the Cu L_3. (B) Cu L_3 X-ray absorption spectrum of $CuBi_2O_4$ indicating the selected photon energies for the resonant photoemission experiment.

of the main valence band, which is consistent with the description of CuO and HTSC cuprates as charge transfer insulators. A very similar spectroscopic structure was found in the Cu 2p resonant photoemission spectrum of CuO.[11,33] Tjeng et al. could satisfactorily reproduce this spectroscopic structure in their 2p resonant photoemission calculations of the Cu 3d spectral weight for a square planar $[CuO_4]^{6-}$ cluster model.[33] Calculations by Tjeng et al. confirmed that the Cu 2p resonance in the VB photoemission primarily derives from a singlet Cu $3d^8$ final state, with peaks at 16.9 and 13.2 eV binding energies containing atomic ^1S and ^1G character, respectively (see Figure 1A). This further confirms the charge transfer nature of CuO that can be translated to $CuBi_2O_4$.

A more detailed picture of the pure Cu 3d contribution to the valence band can be identified by the intensity difference between on- and off-resonance spectra, as shown in Figure 2. Although the main Cu 3d spectral feature resides at energy levels around 13 eV below the Fermi level, the resonance enhancement of the upper valence band indicates a hybridization between Cu 3d and O 2p states, so that partial Cu 3d character is present across the whole spectrum up to the VBM. The spectral structure indicated at the top of the valence band can be associated with a Zhang−Rice (Z−R) singlet final state ($3d^9\underline{L}$, $\underline{L}$ = O 2p hole), which is the first ionization state in the $[CuO_4]^{6-}$ cluster model.[8−10] The Cu 2p resonant enhancement of the top of the valence band spectrum depicts its partial d^8 final state character, which is consistent with the hybridization of a primer $3d^9\underline{L}$ final state with a d^8 final state, required for the stabilization of the Zhang−Rice final state.[13,33]

https://dx.doi.org/10.1021/acs.jpcc.0c08455
J. Phys. Chem. C 2020, 124, 22416−22425

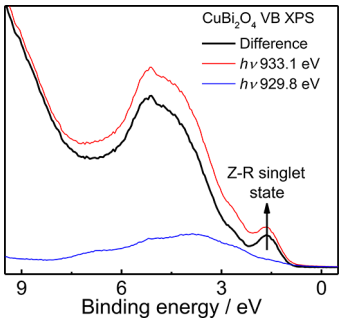

Figure 2. Valence band photoemission of $CuBi_2O_4$ near the Fermi level showing the spectral intensity difference between on-resonance (at $h\nu$ = 933.1 eV) and off-resonance (at $h\nu$ = 929.8 eV) spectra.

Hard X-ray Valence Band Photoemission: Probing the Contribution of Bi 6s and Bi 6p to the VB. The photoemission spectrum of $CuBi_2O_4$ in the valence band region measured with an Al Kα_1 lab X-ray source (1486.6 eV), as well as those measured with 4068 and 8133 eV at a synchrotron, is shown in Figure 3A. The main valence band has a spectral onset at about 0.7 eV and expands up to 8 eV in binding energy. In addition, a broad peak is found on the high binding energy side of the main valence band, centered at 12 eV binding energy. Four spectral features, labeled I, II, III, and IV, can be identified in the main valence band region. The intensity of II and IV relative to I and III continuously increases while moving from soft to hard X-ray ionization photon energy ($h\nu$), resulting in a marked change in the shape of the VB spectrum. At the same time, switching from soft to hard X-ray $h\nu$ leads to a marked increase in the relative intensity of the broad satellite feature at the high binding energy side.

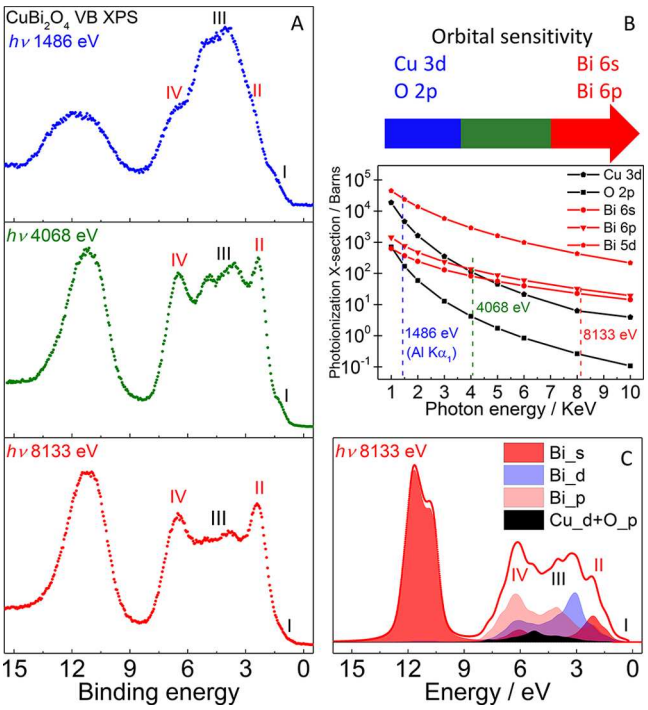

Figure 3. (A) Experimental VB photoemission spectra of $CuBi_2O_4$ measured with 1486 eV (Al Kα_1), 4068 eV, and 8133 eV ionizing photon energy. (B) Photoionization cross section dependence on the ionizing photon energy for valence orbitals in $CuBi_2O_4$.[27] (C) Calculated VB photoemission spectra of $CuBi_2O_4$ at 8133 eV ionizing photon energy.

It is important to note that despite differences in probing depth inherent to soft (surface) and hard (bulk) X-ray photoemission spectroscopies, all features can be clearly observed in all spectra. Therefore, we argue that these features are intrinsic to the material rather than due to surface defects. The observed changes in the VB spectral feature originate from the $h\nu$-dependence of the photoionization cross section of the atomic orbitals contributing to the valence levels. For $CuBi_2O_4$, the valence band is mainly O 2p, with contributions from Cu 3d, Bi 6s, and Bi 6p due to a certain degree of covalency in the bonds, as detailed in our DFT modeling of the electronic structure shown in Figure S5 (SI). However, due to a large photoionization cross section, Cu 3d photoelectrons dominate the spectral features of the soft X-ray spectrum (see Figure 3B). In fact, calculations of the Cu 3d spectral weight, using a $[CuO_4]^{6-}$ cluster with D_{4h} symmetry, have been shown to reproduce fairly well the spectral features observed in the Al Kα VB photoemission spectrum of $CuBi_2O_4$.[13,14] From those calculations and in accordance with our previous discussion, feature I at the top of the VB spectrum can be assigned to the Cu 3d−O 2p hybrid with the Zhang−Rice final state, which has not been observed previously in the photoemission spectrum of $CuBi_2O_4$, probably due to insufficient spectral sensitivity and resolution. Furthermore, as discussed above, the high binding energy broad feature can be partially assigned to Cu 3d with d^8 final states; however, such a satellite feature is also observed in valence band photoemission spectra of Bi-based oxides and is assigned to the main contribution from Bi 6s.[34,35]

As shown in Figure 3B, the photoionization cross section values for O 2p and Cu 3d decrease much faster than those of Bi 6s, Bi 6p, and Bi 5d, and as a result, calculations of the Cu 3d spectral weight using a $[CuO_4]^{6-}$ cluster cannot reproduce the hard X-ray photoemission spectrum because Bi 6s, Bi 6p, and Bi 5d states dominate most spectral features. The evolution of the valence band spectrum as the ionization photon energy is shifted from the soft to the hard X-ray regime allows us to conclude that the states associated with features II and IV at 2.3 and 6.5 eV, respectively, have pronounced Bi 6s and Bi 6p character hybridized with O 2p. In addition, the sharp increase in relative spectral intensity for the high binding energy broad feature is consistent with its partial assignment to Bi 6s as the main contribution.

In order to support the assignment of the contribution of Bi states to the VB, we have simulated the hard X-ray photoemission spectrum at $h\nu$ 8133 eV using the GALORE code.[26] Cross section weighted partial density of states (PDOS) extracted from band structure calculations, shown in Figure S5 (SI), were summed to generate the simulated spectra shown in Figure 3C. In general terms, the simulation compares well with the measured spectrum and allows us to conclude that feature II (centered at around 2.3 eV) has a pronounced Bi 6s−O 2p character, whereas the spectral feature labeled as IV results from an overlap of VB contributions for Cu 3d and Bi 6p.

An early experimental study of the electronic structure of $CuBi_2O_4$ by Goldoni et al.[14] was based on soft X-ray photoemission and electron energy loss (EEL) spectroscopies. A very low relative value of the Bi 6s and Bi 6p cross sections at soft X-ray energy hindered the direct observation of the

https://dx.doi.org/10.1021/acs.jpcc.0c08455
J. Phys. Chem. C 2020, 124, 22416−22425

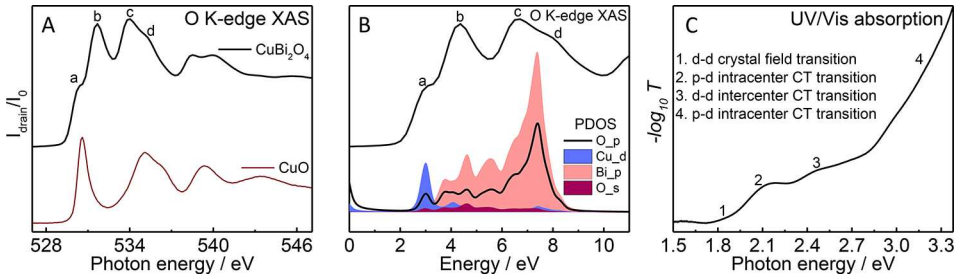

Figure 4. (A) O K-edge XAS of $CuBi_2O_4$ along with that of CuO for comparison. (B) Empty PDOS from DFT calculations for $CuBi_2O_4$; the O K-edge XAS is included in the same scale for comparison. (C) UV−vis absorption spectrum of $CuBi_2O_4$.

contribution of Bi electronic states to the valence band. However, the authors used the interpretation of EEL spectra to conclude that there was a contribution of Bi 6s at the top of the valence band. On the other hand, as shown in our work, hard X-ray excitation energies provide direct observation of the contribution of Bi states within the valence band of $CuBi_2O_4$. Our results reveal that this contribution is deeper in energy into the valence band, with maximum Bi 6s−O 2p hybrid states at 2.3 eV below the Fermi level, leaving the valence band maximum with a predominant Cu 3d−O 2p hybrid character. Therefore, taken together, our results suggest that the electronic structure of $CuBi_2O_4$ can be described within the charge-transfer semiconductor picture, similar to its parent binary oxide CuO.[33,36]

O K-Edge X-ray Absorption. Due to dipole selection rules, the O K-edge XAS probes the transition from O 1s to unoccupied states with partial O 2p character hybridized with Cu 3d, Bi 6s, and Bi 6p states. Theoretical and experimental descriptions of the XAS process have shown that the interaction of valence electrons with the core hole created upon excitation leads to a slight modification of the electronic structure of the final state, which complicates a straightforward comparison of XAS spectra with the ground-state density of states.[37,38] This effect is particularly pronounced for transition-metal L-edge XAS, although detailed calculations of the effect of the O 1s core hole in transition-metal oxides demonstrate that its effect on the band structure is weak. Thus, the O K-edge spectra can be qualitatively related to unoccupied density of states of primarily transition-metal character, provided there is enough hybridization with O 2p to generate measurable oscillator strength.[39] The O K-edge XAS of $CuBi_2O_4$, shown in Figure 4A, has an onset at 529.6 eV and the main absorption expands up to 537.5 eV. Four features can be seen in the main absorption spectrum, as indicated in Figure 4A with letters a−d. By comparing with the O K-edge XAS of CuO, we tentatively assign the onset feature a to be Cu 3d−O 2p hybrid states at the bottom of the conduction band.

In order to assign the contribution of Bi states to the conduction band of $CuBi_2O_4$, we directly compare our experimental O K-edge XAS spectrum to the corresponding hybrid DFT-calculated PDOS in Figure 4B. To make the comparison illustrative, we shifted the spectrum onset to match that of empty states in the DFT calculations. The comparison confirms the Cu 3d character of spectral feature a at the conduction band minimum (CBM), whereas features b−d, located at higher energy levels, can be mostly related to Bi 6p−O 2p hybrid states.

Together with the photoemission study of the valence band, showing that the VBM is predominantly a Cu 3d−O 2p hybrid electronic state, our results provide more insights into the optical absorption spectrum of $CuBi_2O_4$, shown in Figure 4C. Previous reports have argued that the weak optical absorption observed at 1.8 eV arises from the band gap absorption.[2−4] However, since the lowest-energy optical absorption arises from the transition from the VBM of mixed O 2p/Cu 3d character to the empty Cu 3d e_g state, our results suggest that the weak visible absorption onset is most probably due to a low cross section parity-forbidden crystal field d−d transition. Apart from this weak transition, charge-transfer (CT) transitions previously identified for $CuBi_2O_4$ can been seen in the UV−vis spectrum of our sample at 2.08 eV (p−d intracenter CT transition), 2.55 eV (d−d intercenter CT transitions), and >3.2 eV (p−d intracenter CT transition).[40] Charge-transfer transitions can be associated with the band gap excitation in $CuBi_2O_4$, which is an indirect transition, according to our band structure diagram along high-symmetry points of the Brillouin zone (see Figure S5, SI). Although one major asset of $CuBi_2O_4$ for photoelectrochemical applications is its low onset of visible-light absorption, it shows negligible photochemical activity under low-energy visible-light irradiation. For instance, it has been shown that the incident photon to current efficiency (IPCE) is negligible for $h\nu \leq 2.25$ eV,[3] and we have recently shown that the surface photoreduction of $CuBi_2O_4$ does not proceed when irradiated with $h\nu \leq 2.30$ eV.[41] These observations are consistent with the localized nature of the low-energy optical transitions. Low-energy visible-light absorption associated with a parity-forbidden crystal field d−d transition has also been observed in large band gap Cu(II)-based oxides, such as $CuWO_4$ and $CaCu_3Ti_4O_{12}$.[42,43]

Interface Energetics in $CuBi_2O_4$ and Choice of Contact Materials. As discussed above, although both Bi 6s and Cu 3d contribute to the valence band via hybridization with O 2p, the VBM of $CuBi_2O_4$ can be described as O 2p with significant contribution from Cu 3d and negligible contribution from Bi 6s. Likewise, the CBM is predominantly empty Cu 3d hybridized with O 2p, providing this material with a chemistry similar to that of the parent compound CuO. In fact, the material properties of $CuBi_2O_4$ are closely related to those of CuO; e.g., both materials exhibit p-type semiconductivity[2,44] and behave as cathodes in photoelectrochemical cells.[3,45] Both materials present a characteristic low carrier (hole) mobility, $<10^{-2}$ cm^2 V^{-1} s^{-1},[3,46,47] which is detrimental to PEC applications of these materials. However, as described in detail below, the ionization potential (IP) of $CuBi_2O_4$ is larger than that of CuO.

We have explored the electron energy levels in $CuBi_2O_4$ relative to other more common p-type semiconductor oxides, such as CuO and NiO, by determining their IPs via photoemission spectroscopy. To this end, we measured the

https://dx.doi.org/10.1021/acs.jpcc.0c08455
J. Phys. Chem. C 2020, 124, 22416−22425

work function (Φ_w) by determining the difference between the width of the photoemission spectrum and the source energy (Figure S4, SI). Then, the IP was estimated from the onset of the valence band spectrum, considering that IP = Φ_w + VBM. An estimation of the conduction band minimum (or electron affinity) can be obtained from the reported optical band gaps of these materials, i.e., 1.44 eV for CuO,[20] 3.7 eV for NiO,[19,48] and 1.8 eV for $CuBi_2O_4$.[2−4,41]

Using this information, we constructed schematics of the band energy levels relative to the vacuum level for $CuBi_2O_4$, CuO, and NiO (see Figure 5A). In order to support the

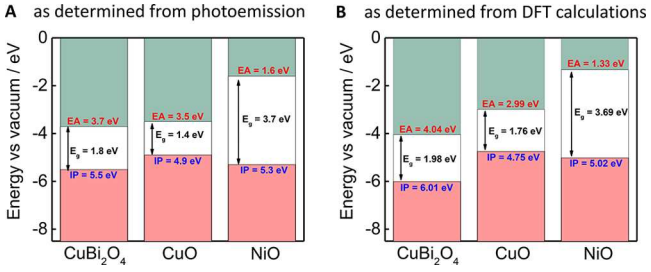

Figure 5. (A) Measured and (B) calculated electron affinity (CBM) and ionization potential (VBM) of $CuBi_2O_4$, CuO, and NiO with respect to the vacuum level.

experimentally determined relative band energy positions, we have also carried out two separate computational analyses on kusachiite $CuBi_2O_4$, cubic CuO, and rock salt NiO: (i) the electronic structures of the bulk crystals and (ii) the absolute vacuum alignment from a well-converged slab-gap model. The band gap of $CuBi_2O_4$ is predicted at 1.98 eV, in close agreement with the current and previous experimentally estimated value of 1.80 eV and the previous DFT+U predicted value of 1.90 eV.[2−4] The standard GGA-PBE functional underestimated the band gap of $CuBi_2O_4$ at 1.05 eV. The band gaps of CuO (1.76 eV) and NiO (3.69 eV) calculated using the HSE06 hybrid functional are consistent with known optical band gaps for CuO (1.3−2.1 eV eV)[49,50] and NiO (3.4−4.3 eV),[51−53] depending on how the location of the band edge is defined: the location of the first absorption feature, the midpoint of the first rise, or where the maximum slope of absorption extrapolates to zero. Previous LDA+U calculations give a band gap of 3.4 eV for NiO.[21] For CuO, previous DFT +U calculations predict the band gap at 1.25 eV, whereas the hybrid functional predicts a band gap of 1.42 eV (for mixing ratio α = 0.15).[21]

$CuBi_2O_4$(101), CuO(111), and NiO(111) were chosen for the slab calculations, as they do not contain dangling bonds and resulted in low-energy, nonpolar terminations (Figures S7−S10, SI). The slabs are constructed of thicknesses larger than 20 Å [24.362 Å for $CuBi_2O_4$(101), 23.805 Å for CuO(111), and 24.304 Å for NiO(111)], and in every simulation cell, a vacuum region of 15 Å perpendicular to the surface was tested to be sufficient to avoid interactions between periodic slabs. The electrostatic potential was averaged along the *c*-direction in order to determine the external vacuum level (see Figures S8−S10, SI), using the MacroDensity package.[23−25] Displayed in Figure 5B are the calculated IP and electron affinity (EA) values of the $CuBi_2O_4$(101), CuO(111), and NiO(111) surfaces. Consistent with the experimental values, the IPs of $CuBi_2O_4$(101), CuO(111), and NiO(111) surfaces were predicted as 6.01, 4.75, and 5.02 eV, whereas the EA values were predicted as 4.04, 2.99, and 0.92 eV, respectively.

There is agreement between measured and simulated values of the electron energetics for each material. In particular, the simulated values reproduce very well the relative energy levels of the CBMs and VBMs of $CuBi_2O_4$, CuO, and NiO, which is the most important parameter that determines the most likely electron transfer in a stacked photoelectrode design. For instance, there has been an increasing interest in using NiO thin films as a hole transport layer in solar energy devices, mainly due to their successful incorporation in hybrid perovskite photovoltaic cells,[54,55] as well as all-oxide transparent diodes.[56,57] However, it is important to consider that NiO must have a smaller ionization potential than the semiconductor photoabsorber coupled to it, in order to form a suitable hole selective contact and behave as a hole transport layer. In this sense, a NiO thin film may act as a hole transport layer for $CuBi_2O_4$-based photoelectrodes, as Lee et al.[58] and Song et al.[59] have shown recently. However, despite the fact that CuO is a well-known photocathode material, coupling a NiO layer to CuO would bring about a detrimental effect to the PEC efficiency of the resulting system, owing to incompatible interface energetics. Therefore, the relative high IP of $CuBi_2O_4$ provides the basis for materials engineering approaches to enhance the hole mobility and transport, which is very important for Cu-based photoelectrodes because of their poor charge carrier transport properties, as described above.

We have carried out a proof-of-concept experiment in which we compared the effect of NiO as a contact layer in CuO- and $CuBi_2O_4$-based photoelectrodes. To achieve this setup, we

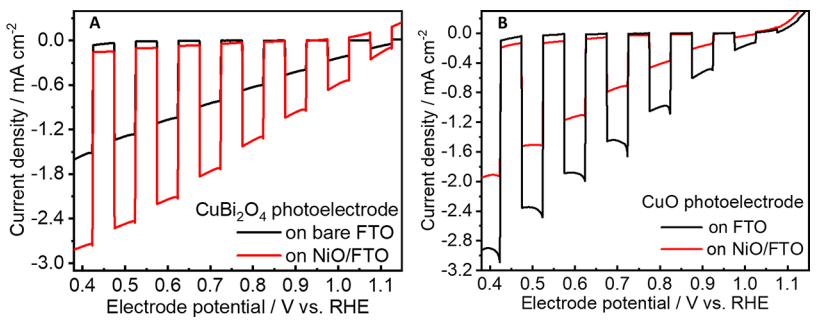

Figure 6. (A) Chopped-light linear sweep voltammetry scans for $CuBi_2O_4$ (black) and NiO/$CuBi_2O_4$ (red) photoelectrodes. (B) Chopped-light linear sweep voltammetry scans for CuO (black) and NiO/CuO (red) photoelectrodes. PEC measurements were done in 0.2 M K_2SO_4 + 0.1 M phosphate buffer solution (pH 6.8) with 0.3% w/w H_2O_2.

https://dx.doi.org/10.1021/acs.jpcc.0c08455
J. Phys. Chem. C 2020, 124, 22416−22425

have developed a multilayer thin film deposition method in order to make photoelectrodes for a comparative photoelectrochemical study. In a first step, NiO thin films were deposited by a sol−gel method on FTO substrates with a pattern defined by a mask. The resulting NiO-patterned FTO substrates were used for an overall spin-coating deposition of CuO and $CuBi_2O_4$, as described in the Experimental Section, so that part of the photoabsorber film is deposited on bare FTO and the other part over NiO/FTO, featuring similar film thicknesses. Figure 6A shows the linear sweep voltammetry scan under chopped illumination of a $CuBi_2O_4$ photocathode on bare FTO (black line) and that of the same material on NiO/FTO (red line). Similarly, Figure 6B shows the photoresponse of CuO deposited on bare FTO and on NiO/FTO. A degassed solution of 200 mM sodium sulfate and 100 mM sodium phosphate buffer at pH 6.8 was used as the electrolyte, with the addition of 50 mM of hydrogen peroxide as an electron scavenger.

A substantial increase in the photoresponse is observed for $CuBi_2O_4$ photocathodes upon introducing NiO as a hole transport layer to the electrode, reaching 2.1 mA cm^{-2} at 0.6 V vs RHE, which is an effect that has been previously observed in $CuBi_2O_4$-based photoelectrodes.[58,59] In contrast, the incorporation of NiO in CuO photoelectrodes causes a detrimental effect that lowers the observed photocurrent by about 50%. The very fast kinetics for H_2O_2 reduction minimizes any catalytic limitation at the surface of the electrode, so the observed increased photoresponse reflects the better charge carrier transport properties of $CuBi_2O_4$−NiO photoelectrodes, in contrast to the detrimental effect in using NiO as the contact layer in CuO photoelectrodes.

CONCLUSION

In this paper, we have reported a detailed study of the electronic structure of $CuBi_2O_4$ based on advanced X-ray spectroscopic techniques: HAXPES, ResPES, and O K-edge X-ray absorption spectroscopy. Owing to the dependence of the relative photoionization cross sections for different electronic orbitals on the ionizing photon energy, soft X-ray photoemission spectroscopy preferentially probes Cu 3d valence states, whereas Bi 6s and Bi 6p make up most of the spectral features in HAXPES. This difference allowed us to identify the Bi and Cu contributions to the valence band by taking VB spectra at different ionization photon energies. On the basis of this strategy, we found that (i) the main Cu 3d spectral feature resides at energy levels around 13 eV below the Fermi level. However, due to the strong hybridization between Cu 3d and O 2p states, Cu 3d character is present across the whole spectrum up to the valence band maximum (VBM). We identified a spectroscopic feature at the top of the VB associated with a Zhang−Rice singlet final state (Cu $3d^9\underline{L}$), which has been predicted for $CuBi_2O_4$ but not observed in previous experimental studies. (ii) There is a strong Bi 6s−O 2p hybrid electronic state with a maximum at 2.3 eV below the Fermi level, although the contribution is negligible at higher binding energies, leaving the VBM with a predominant Cu 3d−O 2p hybrid character. (iii) The CBM has strong Cu 3d character, whereas Bi 6p−O 2p hybrid electronic states make up most of the rest of the conduction band. On the basis of these electronic features, we suggest that the low visible-light absorption at the onset of the absorption feature at $h\nu \sim 1.8$ eV originates from a localized d−d forbidden electronic transition, leading to a low absorption coefficient for visible light and consequent poor photochemical activity under low-energy visible-light irradiation. In addition, a combined experimental and theoretical study of the interface energetics shows that the IP of $CuBi_2O_4$ is higher than that of the related material CuO and that of NiO, which provides a basis for materials engineering approaches to enhance the hole transport, which is critically important for Cu-based photoelectrodes, owing to their poor charge carrier transport properties.

ASSOCIATED CONTENT

Supporting Information

The Supporting Information is available free of charge at https://pubs.acs.org/doi/10.1021/acs.jpcc.0c08455.

X-ray diffraction pattern of $CuBi_2O_4$ films; additional hard X-ray and lab-based X-ray photoemission spectra; secondary energy cutoff plots for work function determination; bulk electronic structure, (partial) density of states, and interface energetics calculations for $CuBi_2O_4$, CuO, and NiO (PDF)

AUTHOR INFORMATION

Corresponding Authors

Freddy E. Oropeza − *Laboratory of Inorganic Materials and Catalysis, Department of Chemical Engineering and Chemistry, Eindhoven University of Technology, 5600 MB Eindhoven, The Netherlands; IMDEA Energy Institute, 28935 Móstoles, Madrid, Spain;* orcid.org/0000-0001-7222-9603; Email: freddy.oropeza@gmail.com

Jan P. Hofmann − *Laboratory of Inorganic Materials and Catalysis, Department of Chemical Engineering and Chemistry, Eindhoven University of Technology, 5600 MB Eindhoven, The Netherlands; Surface Science Laboratory, Department of Materials and Earth Sciences, Technical University of Darmstadt, 64287 Darmstadt, Germany;* orcid.org/0000-0002-5765-1096; Email: hofmann@surface.tu-darmstadt.de

Authors

Nelson Y. Dzade − *School of Chemistry, Cardiff University, CF10 3AT Cardiff, U.K.;* orcid.org/0000-0001-7733-9473

Amalia Pons-Martí − *Laboratory of Inorganic Materials and Catalysis, Department of Chemical Engineering and Chemistry, Eindhoven University of Technology, 5600 MB Eindhoven, The Netherlands*

Zhenni Yang − *State Key Laboratory of Physical Chemistry of Solid Surfaces, College of Chemistry and Chemical Engineering, Xiamen University, Xiamen 361005, P.R. China*

Kelvin H. L. Zhang − *State Key Laboratory of Physical Chemistry of Solid Surfaces, College of Chemistry and Chemical Engineering, Xiamen University, Xiamen 361005, P.R. China;* orcid.org/0000-0001-9352-6236

Nora H. de Leeuw − *School of Chemistry, Cardiff University, CF10 3AT Cardiff, U.K.; School of Chemistry, University of Leeds, Leeds LS2 9JT, U.K.; Department of Earth Sciences, Utrecht University, 3584 CB Utrecht, The Netherlands;* orcid.org/0000-0002-8271-0545

Emiel J. M. Hensen − *Laboratory of Inorganic Materials and Catalysis, Department of Chemical Engineering and Chemistry, Eindhoven University of Technology, 5600 MB Eindhoven, The Netherlands;* orcid.org/0000-0002-9754-2417

Complete contact information is available at: https://pubs.acs.org/10.1021/acs.jpcc.0c08455

https://dx.doi.org/10.1021/acs.jpcc.0c08455
J. Phys. Chem. C 2020, 124, 22416−22425

Notes

The authors declare no competing financial interest.

■ ACKNOWLEDGMENTS

This work was supported by The Netherlands Center for Multiscale Catalytic Energy Conversion (MCEC), an NWO Gravitation program funded by the Ministry of Education, Culture and Science of the government of The Netherlands. K.H.L.Z. is grateful for funding support by the National Science Foundation of China (NSFC) (reference number: 21872116). The synchrotron data shown here were collected during beamtimes SI19191-1 (Diamond) and 20170915 (LNLS). We thank Dr. Tien-Lin Lee and Dr. Pardeep Kumar Thakur (I09 at Diamond), and Dr. Julio Criginski Cezar (PGM at LNLS) for their technical assistance during synchrotron data collection. N.Y.D. and N.H.d.L. thank the Engineering and Physical Sciences Research Council for funding (grants EP/S001395/1 and EP/K009567/2). The calculations were performed using the computational facilities of the Advanced Research Computing @ Cardiff (ARCCA) Division, Cardiff University, and we also acknowledge the use of HPC Wales, Supercomputing Wales, and associated support services in the completion of this work.

■ REFERENCES

(1) Fink, J.; Golden, M. S.; Knupfer, M.; Böske, T.; Haffner, S.; Neudert, R.; Atzkern, S.; Dürr, C.; Hu, Z.; Legner, S.; Pichler, T.; Rosner, H.; Drechsler, S.-L.; Hayn, R.; Málek, J.; Eschrig, H.; Ruck, K.; Krabbes, G. The Electronic Structure of High-Tc Superconductors: Introduction and Recent Studies of Model Compounds. In *High-T_c Superconductors and Related Materials*; Springer Netherlands: Dordrecht, 2001; pp 1−38. DOI: 10.1007/978-94-010-0758-0_1.

(2) Sharma, G.; Zhao, Z.; Sarker, P.; Nail, B. A.; Wang, J.; Huda, M. N.; Osterloh, F. E. Electronic Structure, Photovoltage, and Photocatalytic Hydrogen Evolution with p-$CuBi_2O_4$ Nanocrystals. *J. Mater. Chem. A* **2016**, *4* (8), 2936−2942.

(3) Berglund, S. P.; Abdi, F. F.; Bogdanoff, P.; Chemseddine, A.; Friedrich, D.; van de Krol, R. Comprehensive Evaluation of $CuBi_2O_4$ as a Photocathode Material for Photoelectrochemical Water Splitting. *Chem. Mater.* **2016**, *28* (12), 4231−4242.

(4) Hahn, N. T.; Holmberg, V. C.; Korgel, B. A.; Mullins, C. B. Electrochemical Synthesis and Characterization of P-$CuBi_2O_4$ Thin Film Photocathodes. *J. Phys. Chem. C* **2012**, *116* (10), 6459−6466.

(5) Wang, F.; Septina, W.; Chemseddine, A.; Abdi, F. F.; Friedrich, D.; Bogdanoff, P.; van de Krol, R.; Tilley, S. D.; Berglund, S. P. Gradient Self-Doped $CuBi_2O_4$ with Highly Improved Charge Separation Efficiency. *J. Am. Chem. Soc.* **2017**, *139* (42), 15094−15103.

(6) Janson, O.; Kuzian, R. O.; Drechsler, S. L.; Rosner, H. Electronic Structure and Magnetic Properties of the Spin-1/2 Heisenberg Magnet Bi_2CuO_4. *Phys. Rev. B: Condens. Matter Mater. Phys.* **2007**, *76* (11), 115119.

(7) Di Sante, D.; Hausoel, A.; Barone, P.; Tomczak, J. M.; Sangiovanni, G.; Thomale, R. Realizing Double Dirac Particles in the Presence of Electronic Interactions. *Phys. Rev. B: Condens. Matter Mater. Phys.* **2017**, *96* (12), 121106.

(8) Shen, Z. X.; List, R. S.; Dessau, D. S.; Parmigiani, F.; Arko, A. J.; Bartlett, R.; Wells, B. O.; Lindau, I.; Spicer, W. E. Photoemission Study of CuO and Cu_2O Single Crystals. *Phys. Rev. B: Condens. Matter Mater. Phys.* **1990**, *42* (13), 8081−8085.

(9) Sarma, D. D.; Sreedhar, K. Electronic Structure of Square Planar CuO_4^{6-} Clusters. *Z. Phys. B: Condens. Matter* **1988**, *69* (4), 529−534.

(10) Eskes, H.; Tjeng, L. H.; Sawatzky, G. A. Cluster-Model Calculation of the Electronic Structure of CuO: A Model Material for the High-Tc Superconductors. *Phys. Rev. B: Condens. Matter Mater. Phys.* **1990**, *41* (1), 288−299.

(11) Tjeng, L. H.; Sinkovic, B.; Brookes, N. B.; Goedkoop, J. B.; Hesper, R.; Pellegrin, E.; De Groot, F. M. F.; Altieri, S.; Hulbert, S. L.; Shekel, E.; Sawatzky, G. A. Spin-Resolved Photoemission on Anti-Ferromagnets: Direct Observation of Zhang-Rice Singlets in CuO. *Phys. Rev. Lett.* **1997**, *78* (6), 1126−1129.

(12) Ghijsen, J.; Tjeng, L. H.; Eskes, H.; Sawatzky, G. A.; Johnson, R. L. Resonant Photoemission Study of the Electronic Structure of CuO and Cu_2O. *Phys. Rev. B: Condens. Matter Mater. Phys.* **1990**, *42* (4), 2268−2274.

(13) Parmigiani, F.; Sangaletti, L. Behaviour of the Zhang-Rice Singlet in $CuGeO_3$, Bi_2CuO_4, and CuO. *J. Electron Spectrosc. Relat. Phenom.* **2000**, *107* (1), 49−62.

(14) Goldoni, A.; Del Pennino, U.; Parmigiani, F.; Sangaletti, L.; Revcolevschi, A. Electronic Structure of Bi_2CuO_4. *Phys. Rev. B: Condens. Matter Mater. Phys.* **1994**, *50* (15), 10435−10441.

(15) Lee, T.-L.; Duncan, D. A. A Two-Color Beamline for Electron Spectroscopies at Diamond Light Source. *Synchrotron Radiat. News* **2018**, *31* (4), 16−22.

(16) Kresse, G.; Furthmüller, J. Efficiency of Ab-Initio Total Energy Calculations for Metals and Semiconductors Using a Plane-Wave Basis Set. *Comput. Mater. Sci.* **1996**, *6* (1), 15−50.

(17) Blöchl, P. E. Projector Augmented-Wave Method. *Phys. Rev. B: Condens. Matter Mater. Phys.* **1994**, *50* (24), 17953−17979.

(18) Perdew, J. P.; Burke, K.; Ernzerhof, M. Generalized Gradient Approximation Made Simple. *Phys. Rev. Lett.* **1996**, *77* (18), 3865−3868.

(19) Zhang, J. Y.; Li, W. W.; Hoye, R. L. Z.; MacManus-Driscoll, J. L.; Budde, M.; Bierwagen, O.; Wang, L.; Du, Y.; Wahila, M. J.; Piper, L. F. J.; Lee, T. L.; Edwards, H. J.; Dhanak, V. R.; Zhang, K. H. L. Electronic and Transport Properties of Li-Doped NiO Epitaxial Thin Films. *J. Mater. Chem. C* **2018**, *6* (9), 2275−2282.

(20) Wang, Y.; Lany, S.; Ghanbaja, J.; Fagot-Revurat, Y.; Chen, Y. P.; Soldera, F.; Horwat, D.; Mücklich, F.; Pierson, J. F. Electronic Structures of Cu_2O, Cu_4O_3, and CuO: A Joint Experimental and Theoretical Study. *Phys. Rev. B: Condens. Matter Mater. Phys.* **2016**, *94* (24), 245418.

(21) Shick, A. B.; Liechtenstein, A. I.; Pickett, W. E. Implementation of the LDA+U Method Using the Full-Potential Linearized Augmented Plane-Wave Basis. *Phys. Rev. B: Condens. Matter Mater. Phys.* **1999**, *60* (15), 10763−10769.

(22) Živković, A.; Roldan, A.; de Leeuw, N. H. Density Functional Theory Study Explaining the Underperformance of Copper Oxides as Photovoltaic Absorbers. *Phys. Rev. B: Condens. Matter Mater. Phys.* **2019**, *99* (3), 035154.

(23) Walsh, A.; Butler, K. T. Prediction of Electron Energies in Metal Oxides. *Acc. Chem. Res.* **2014**, *47* (2), 364−372.

(24) Burton, L. A.; Walsh, A. Band Alignment in SnS Thin-Film Solar Cells: Possible Origin of the Low Conversion Efficiency. *Appl. Phys. Lett.* **2013**, *102* (13), 132111.

(25) Yang, R. X.; Butler, K. T.; Walsh, A. Assessment of Hybrid Organic-Inorganic Antimony Sulfides for Earth-Abundant Photovoltaic Applications. *J. Phys. Chem. Lett.* **2015**, *6* (24), 5009−5014.

(26) Jackson, A. J.; Ganose, A. M.; Regoutz, A.; Egdell, R. G.; Scanlon, D. O. Galore: Broadening and Weighting for Simulation of Photoelectron Spectroscopy. *J. Open Source Softw.* **2018**, *3* (26), 773.

(27) Scofield, J. H. *Theoretical Photoionization Cross Sections from 1 to 1500 keV*; U.S. Atomic Energy Commission, 1973. DOI: 10.2172/4545040.

(28) Gelius, U.; Siegbahn, K. ESCA Studies of Molecular Core and Valence Levels in the Gas Phase. *Faraday Discuss. Chem. Soc.* **1972**, *54* (0), 257−268.

(29) Gelius, U. Recent Progress in ESCA Studies of Gases. *J. Electron Spectrosc. Relat. Phenom.* **1974**, *5* (1), 985−1057.

(30) Böske, T.; Maiti, K.; Knauff, O.; Ruck, K.; Golden, M.; Krabbes, G.; Fink, J.; Osafune, T.; Motoyama, N.; Eisaki, H.; Uchida, S. Cu-O Network-Dependent Core-Hole Screening in Low-Dimensional Cuprate Systems: A High-Resolution x-Ray Photoemission

https://dx.doi.org/10.1021/acs.jpcc.0c08455
J. Phys. Chem. C 2020, 124, 22416−22425

Study. *Phys. Rev. B: Condens. Matter Mater. Phys.* **1998**, *57* (1), 138−141.
(31) Waidacher, C.; Richter, J.; Becker, K. Cu-O Network-Dependent Core-Hole Screening in Low-Dimensional Cuprates: A Theoretical Analysis. *Phys. Rev. B: Condens. Matter Mater. Phys.* **2000**, *61* (20), 13473−13479.
(32) Allen, J. W. Resonant Photoemission of Solids with Strongly Correlated Electrons. In *Synchrotron Radiation Research*; Springer: Boston, 1992; Vol. *1*, pp 253−323. DOI: 10.1007/978-1-4615-3280-4_6.
(33) Tjeng, L. H.; Chen, C. T.; Ghijsen, J.; Rudolf, P.; Sette, F. Giant Cu 2*p* Resonances in CuO Valence-Band Photoemission. *Phys. Rev. Lett.* **1991**, *67* (4), 501−504.
(34) Payne, D. J.; Robinson, M. D. M.; Egdell, R. G.; Walsh, A.; McNulty, J.; Smith, K. E.; Piper, L. F. J. The Nature of Electron Lone Pairs in $BiVO_4$. *Appl. Phys. Lett.* **2011**, *98* (21), 212110.
(35) Walsh, A.; Watson, G. W.; Payne, D. J.; Edgell, R. G.; Guo, J.; Glans, P.-A.; Learmonth, T.; Smith, K. E. Electronic Structure of the α and δ Phases of Bi_2O_3: A Combined *Ab Initio* and x-Ray Spectroscopy Study. *Phys. Rev. B: Condens. Matter Mater. Phys.* **2006**, *73* (23), 235104.
(36) Ghijsen, J.; Tjeng, L. H.; Eskes, H.; Sawatzky, G. A.; Johnson, R. L. Resonant Photoemission Study of the Electronic Structure of CuO and Cu_2O. *Phys. Rev. B: Condens. Matter Mater. Phys.* **1990**, *42* (4), 2268−2274.
(37) Kurmaev, E. Z.; Wilks, R. G.; Moewes, A.; Finkelstein, L. D.; Shamin, S. N.; Kuneš, J. Oxygen X-Ray Emission and Absorption Spectra as a Probe of the Electronic Structure of Strongly Correlated Oxides. *Phys. Rev. B: Condens. Matter Mater. Phys.* **2008**, *77* (16), 165127.
(38) Mauchamp, V.; Jaouen, M.; Schattschneider, P. Core-Hole Effect in the One-Particle Approximation Revisited from Density Functional Theory. *Phys. Rev. B: Condens. Matter Mater. Phys.* **2009**, *79* (23), 235106.
(39) Huang, X. C.; Zhang, J. Y.; Wu, M.; Zhang, S.; Xiao, H. Y.; Han, W. Q.; Lee, T. L.; Tadich, A.; Qi, D. C.; Qiao, L.; Chen, L.; Zhang, K. H. L. Electronic Structure and p -Type Conduction Mechanism of Spinel Cobaltite Oxide Thin Films. *Phys. Rev. B: Condens. Matter Mater. Phys.* **2019**, *100* (11), 115301.
(40) Pisarev, R. V.; Pavlov, V. V.; Kalashnikova, A. M.; Moskvin, A. S. Near-Band Gap Electronic Structure of the Tetragonal Rare-Earth Cuprates R_2CuO_4 and the Bismuth Cuprate Bi_2CuO_4. *Phys. Rev. B: Condens. Matter Mater. Phys.* **2010**, *82* (22), 224502.
(41) Oropeza, F. E.; Feleki, B. T.; Zhang, K. H. L.; Hensen, E. J. M.; Hofmann, J. P. Influence of Reduced Cu Surface States on the Photoelectrochemical Properties of $CuBi_2O_4$. *ACS Appl. Energy Mater.* **2019**, *2* (9), 6866−6874.
(42) Tian, C. M.; Jiang, M.; Tang, D.; Qiao, L.; Xiao, H. Y.; Oropeza, F. E.; Hofmann, J. P.; Hensen, E. J. M.; Tadich, A.; Li, W.; Qi, D. C.; Zhang, K. H. L. Elucidating the Electronic Structure of $CuWO_4$ Thin Films for Enhanced Photoelectrochemical Water Splitting. *J. Mater. Chem. A* **2019**, *7* (19), 11895−11907.
(43) Clark, J. H.; Dyer, M. S.; Palgrave, R. G.; Ireland, C. P.; Darwent, J. R.; Claridge, J. B.; Rosseinsky, M. J. Visible Light Photo-Oxidation of Model Pollutants Using $CaCu_3Ti_4O_{12}$: An Experimental and Theoretical Study of Optical Properties, Electronic Structure, and Selectivity. *J. Am. Chem. Soc.* **2011**, *133* (4), 1016−1032.
(44) Jeong, Y. K.; Choi, G. M. Nonstoichiometry and Electrical Conduction of CuO. *J. Phys. Chem. Solids* **1996**, *57* (1), 81−84.
(45) Septina, W.; Prabhakar, R. R.; Wick, R.; Moehl, T.; Tilley, S. D. Stabilized Solar Hydrogen Production with CuO/CdS Heterojunction Thin Film Photocathodes. *Chem. Mater.* **2017**, *29* (4), 1735−1743.
(46) Samokhvalov, A. A.; Viglin, N. A.; Gizhevskii, B. A.; Loshkareva, N. N.; Osipov, V. V.; Solin, N. I.; Sukhorukov, Y. P. Low-Mobility Charge Carriers in CuO. *Zh. Eksp. Teor. Fiz.* **1993**, *103*, 951−961.
(47) Tombak, A.; Benhaliliba, M.; Ocak, Y. S.; Kiliçoglu, T. The Novel Transparent Sputtered P-Type CuO Thin Films and Ag/p-CuO/n-Si Schottky Diode Applications. *Results Phys.* **2015**, *5*, 314−321.
(48) Fu, G.; Wen, X.; Xi, S.; Chen, Z.; Li, W.; Zhang, J. Y.; Tadich, A.; Wu, R.; Qi, D. C.; Du, Y.; Cheng, J.; Zhang, K. H. L. Tuning the Electronic Structure of NiO via Li Doping for the Fast Oxygen Evolution Reaction. *Chem. Mater.* **2019**, *31* (2), 419−428.
(49) Dahrul, M.; Alatas, H.; Irzaman. Preparation and Optical Properties Study of CuO Thin Film as Applied Solar Cell on LAPAN-IPB Satellite. *Procedia Environ. Sci.* **2016**, *33*, 661−667.
(50) Murali, D. S.; Kumar, S.; Choudhary, R. J.; Wadikar, A. D.; Jain, M. K.; Subrahmanyam, A. Synthesis of Cu_2O from CuO Thin Films: Optical and Electrical Properties. *AIP Adv.* **2015**, *5* (4), 047143.
(51) Powell, R. J.; Spicer, W. E. Optical Properties of NiO and CoO. *Phys. Rev. B* **1970**, *2* (6), 2182−2193.
(52) Hüfner, S. Electronic Structure of NiO and Related 3d-Transition-Metal Compounds. *Adv. Phys.* **1994**, *43* (2), 183−356.
(53) Ismail, R. A.; Ghafori, S.; Kadhim, G. A. Preparation and Characterization of Nanostructured Nickel Oxide Thin Films by Spray Pyrolysis. *Appl. Nanosci.* **2013**, *3* (6), 509−514.
(54) Liu, Z.; Zhu, A.; Cai, F.; Tao, L.; Zhou, Y.; Zhao, Z.; Chen, Q.; Cheng, Y.-B.; Zhou, H. Nickel Oxide Nanoparticles for Efficient Hole Transport in p-i-n and n-i-p Perovskite Solar Cells. *J. Mater. Chem. A* **2017**, *5* (14), 6597−6605.
(55) Schulz, P.; Cahen, D.; Kahn, A. Halide Perovskites: Is It All about the Interfaces? *Chem. Rev.* **2019**, *119* (5), 3349−3417.
(56) Zhang, J.; Han, S.; Luo, W.; Xiang, S.; Zou, J.; Oropeza, F. E.; Gu, M.; Zhang, K. H. L. Interface Energy Band Alignment at the All-Transparent p-n Heterojunction Based on NiO and $BaSnO_3$. *Appl. Phys. Lett.* **2018**, *112* (17), 171605.
(57) Zhang, K. H. L.; Wu, R.; Tang, F.; Li, W.; Oropeza, F. E.; Qiao, L.; Lazarov, V. K.; Du, Y.; Payne, D. J.; MacManus-Driscoll, J. L.; Blamire, M. G. Electronic Structure and Band Alignment at the NiO and $SrTiO_3$ p-n Heterojunctions. *ACS Appl. Mater. Interfaces* **2017**, *9* (31), 26549−26555.
(58) Lee, J.; Yoon, H.; Kim, S.; Seo, S.; Song, J.; Choi, B.-U.; Choi, S. Y.; Park, H.; Ryu, S.; Oh, J.; Lee, S. Long-Term Stabilized High-Density $CuBi_2O_4$ /NiO Heterostructure Thin Film Photocathode Grown by Pulsed Laser Deposition. *Chem. Commun.* **2019**, *55* (83), 12447−12450.
(59) Song, A.; Plate, P.; Chemseddine, A.; Wang, F.; Abdi, F. F.; Wollgarten, M.; van de Krol, R.; Berglund, S. P. Cu:NiO as a Hole-Selective Back Contact to Improve the Photoelectrochemical Performance of $CuBi_2O_4$ Thin Film Photocathodes. *J. Mater. Chem. A* **2019**, *7* (15), 9183−9194.

https://dx.doi.org/10.1021/acs.jpcc.0c08455
J. Phys. Chem. C 2020, 124, 22416−22425